ACS APPLIED MATERIALS & INTERFACES

Research Article

www.acsami.org

Sulfonic Acid-Functionalized α-Zirconium Phosphate Single-Layer Nanosheets as a Strong Solid Acid for Heterogeneous Catalysis Applications

Yingjie Zhou,[†,‡] Rongcai Huang,[†] Fuchuan Ding,[†] Alex D. Brittain,[†] Jingjing Liu,[†] Meng Zhang,[‡] Min Xiao,[‡] Yuezhong Meng,*[,‡] and Luyi Sun*[,†]

[†]Department of Chemical & Biomolecular Engineering and Polymer Program, Institute of Materials Science, University of Connecticut, Storrs, Connecticut 06269, United States

[‡]The Key Laboratory of Low-carbon Chemistry & Energy Conservation of Guangdong Province/State Key Laboratory of Optoelectronic Materials and Technologies, Sun Yat-sen University, Guangzhou 510275, P. R. China

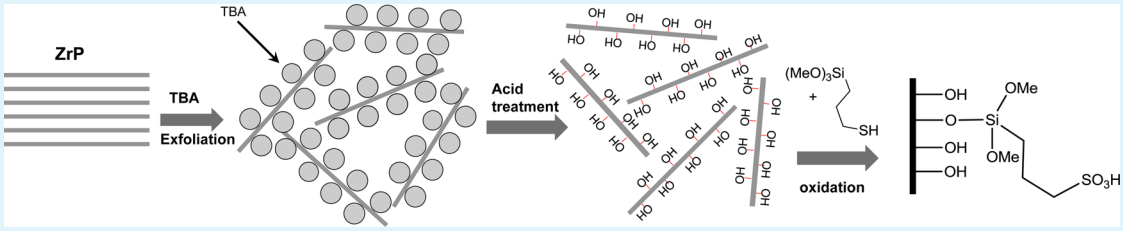

ABSTRACT: Solid acids have received considerable attention as alternatives to traditional corrosive and hazardous homogeneous acids because of their advantages in practical applications, including their low corrosion of equipment and high catalytic activity and recyclability. In this work, a strong solid acid was prepared by anchoring thiol group terminated chains on layered α-zirconium phosphate (ZrP) single-layer nanosheets, followed by oxidation of thiol groups to form sulfonic acid groups. The obtained solid acids were thoroughly characterized and the results proved that sulfonic acid group terminated chains were successfully grafted onto the ZrP nanosheets with a high loading density. Such a strong solid acid based on inorganic nanosheets can be well-dispersed in polar solvents, leading to high accessibility to the acid functional groups. Meanwhile, it can be easily separated from the dispersion system by centrifugation or filtration. The strong solid acid can serve as an effective heterogeneous catalyst for various reactions, including the Bayer–Villiger oxidation of cyclohexanone to ε-caprolactone in the absence of organic solvents.

KEYWORDS: *solid acid, α-zirconium phosphate, heterogeneous catalysis, Baeyer–Villiger oxidation*

1. INTRODUCTION

Solid acid catalysts have received high attention because of their wide applications in chemical industry, including oil refining, petrochemical processes, fuel cells, and separation technologies.[1−3] The traditional corrosive and hazardous homogeneous acid catalysts, such as HF, H_2SO_4, $HClO_4$, and H_3PO_4, have been gradually replaced by solid acids because of their advantages including low corrosion of equipment, high catalytic activity and recyclability, simple handling requirements, and environmentally friendly nature.[4−7]

Recently, huge efforts have been focused on the preparation and characterization of various strong solid acid catalysts,[2,3] such as heteropoly acids, sulfated metal oxides, and organic–inorganic composite catalysts. They have been widely applied in acid-catalyzed reactions, including esterification, isomerization, and Friedel–Crafts reactions,[1,8−10] and exhibit higher performance than the commonly used industrial solid acid catalysts, which typically possess a relatively low acid strength. However, heteropoly acids and sulfated metal oxides suffer from drawbacks such as complicated preparation procedures, low surface areas, and short catalytic lives, which limit their practical applications.[3] Organic-inorganic composite catalysts possess the combined advantages of controllable functionality of organic components and thermally stable and robust inorganic components. Sulfonic acid–based solid acid resins, such as Nafion and Amberlyst, are representative organic components in composite catalysts.[11−13] However, the resin particles are usually entrapped within a porous inorganic network without covalent bonding with the inorganic phase. Their relatively low concentration of acidic sites, aggregations of resin particles, poor porosity, and low accessibility of active sites largely limit them to be used as an efficient catalyst in acid-catalyzed reactions.[11,12,14] Therefore, the synthesis of solid acids with a simple preparation process, strong acidic strength, high acid site concentration, abundant porosity, and easy accessibility of acid sites are highly desirable.

The post-grafting of thiol or acid functionalized organosilanes on porous inorganic matrices is a common method to

Received: February 9, 2014
Accepted: April 7, 2014
Published: April 7, 2014

   dx.doi.org/10.1021/am5008408 | ACS Appl. Mater. Interfaces 2014, 6, 7417−7425

Scheme 1. (a) Preparation of ZrP Single-Layer Nanosheets; (b) Grafting Reaction on the Surface of ZrP Single-Layer Nanosheets

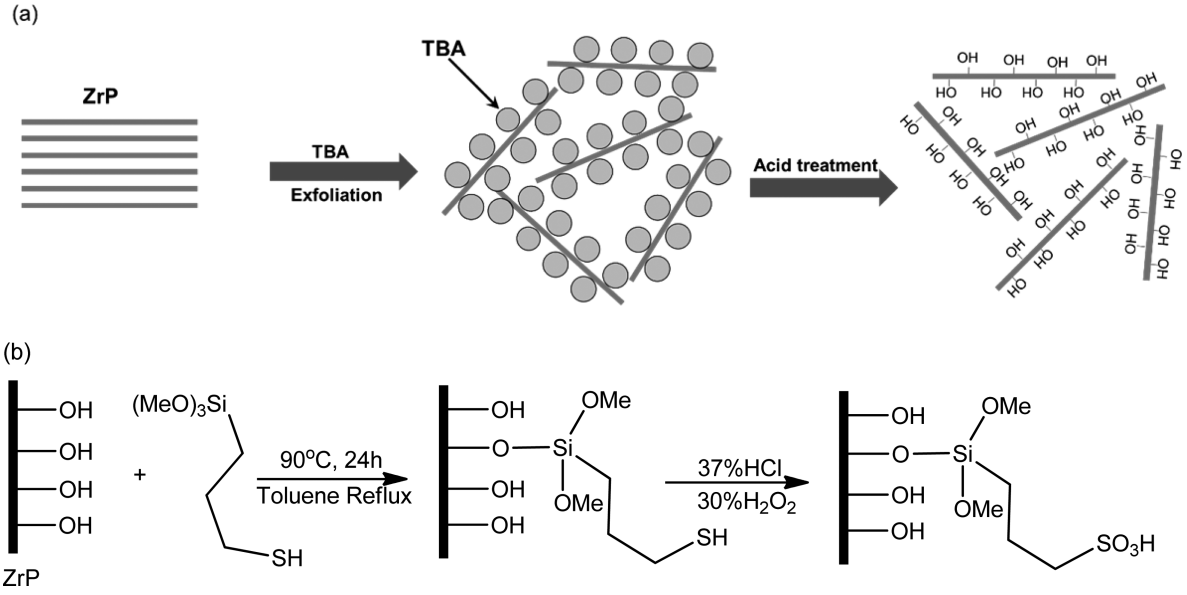

prepare organic-inorganic composite catalysts and it involves the condensation reaction between the hydroxyl groups on the surface of inorganic materials and the alkoxyl- or chloro-silanes groups of organic molecules.[15,16] Up to now, the main choices of inorganic matrices are porous zeolites, silica, and metal oxides.[16−19] However, the limited active sites on regular solid supports surface prohibits a high loading density of functional groups, which comprises their catalytic performances. Compared to porous materials, certain layered materials, such as α-zirconium phosphate (ZrP, $Zr(HPO_4)_2{\cdot}H_2O$), are another group of promising candidates for post-grafting because of the high hydroxyl group density and activity on their surface.[20] While layered ZrP micro-crystals might not be as ideal as porous materials considering the large number of hydroxyl groups within the gallery are not very accessible, single-layer ZrP nanosheets from the exfoliation of ZrP micro-crystals serve as an ideal candidate for post-grafting since after exfoliation, the hydroxyl groups are fully exposed and readily react with silanes. The surface hydroxyl group density on ZrP is ca. 4.2 groups/nm^2 per side (hydroxyl groups existing on both sides of ZrP nanosheets).[21] After surface grafting, the obtained compounds are expected to possess a high density of functional groups, which is critical for high catalytic performance. Moreover, the lateral dimension of ZrP nanosheets can be altered by tuning the synthetic conditions.[22−24] Another major advantage of using ZrP nanosheets as the solid substrate lies in that such nanosheets can be uniformly dispersed in a wide range of polar solvents, leading to high catalytic efficiency, but meanwhile they can be easily separated from the dispersion system using centrifugation, etc. The versatile properties of ZrP have been well studied and it has been applied for various applications[25−33] thanks to its low cost and ease of synthesis. Therefore, the covalent immobilization of acid functional groups on ZrP single-layer nanosheets offers a striking and practical method for facile preparation of heterogeneous solid acid catalysts with promising applications.[34]

In this work, we explored a strong solid acid by anchoring a high density of thiol groups on single layer ZrP nanosheets, which were subsequently oxidized to sulfonic acid groups. The obtained strong solid acids were investigated as heterogeneous catalysts for the Bayer−Villiger oxidation of cyclohexane to ε-caprolactone with H_2O_2 as an oxidant.

2. EXPERIMENTAL SECTION

2.1. Materials. Zirconyl chloride octahydrate ($ZrOCl_2{\cdot}8H_2O$, 98%, Aldrich), phosphoric acid (85%, Aldrich), tetra-*n*-butylammonium hydroxide (TBA, Aldrich), γ-propyl mercaptotrimethoxysilane (MPTMS, Aldrich), hydrogen peroxide (H_2O_2, 30 wt %, Fisher), and cyclohexanone (99%, Alfa Aesar) were used as received. Reagent-grade ethanol, hydrochloric acid (HCl, 37 wt %), toluene, acetone, and acetonitrile were obtained from common commercial sources and used as received.

2.2. Preparation of Single-Layer ZrP Nanosheets. ZrP microcrystals were synthesized according to a previously described process.[22] A sample of 6.0 g of $ZrOCl_2{\cdot}8H_2O$ was mixed with 60.0 mL of 6.0 M H_3PO_4 in a sealed Teflon-lined pressure vessel, and the mixture was reacted at 200 °C for 24 h. Then, the prepared ZrP microcrystals (0.10 g in 6.7 mL of water) were exfoliated by TBA (3.3 mL of 0.10 M aqueous solution) in an ice bath. The exfoliated ZrP nanosheets were treated with 3.3 mL of 0.10 M HCl to regenerate the protonated ZrP single layer nanosheets.[35−37] The thickness of a single layer ZrP nanosheet is ca. 6.3 Å.[23,38] A gelatinous precipitate of the ZrP nanosheets was collected by centrifugation and washed with water to eliminate chloride ions under vigorous stirring. The obtained ZrP nanosheets gel was then washed with acetone and centrifuged to exchange the solvent from water to acetone. This process was repeated 3 times to ensure most water was removed. Subsequently, the ZrP nanosheets gel in acetone was treated by toluene based on the same procedures and the process was repeated 3 times. This eventually led to the formation of ZrP nanosheets in toluene with the assistance of ultrasonication.

2.3. Functionalization of ZrP Nanosheets. ZrP single-layer nanosheets were functionalized via the post-grafting method via the condensation reaction between the hydroxyl groups on individual ZrP nanosheets surface and the methoxysilane groups of MPTMS.[15] In a 500 mL flask equipped with a condenser, 300 mL of ZrP suspension (in toluene, containing 0.90 g of ZrP) was mixed with 14.73 g (75 mmol) of MPTMS. The dispersion was refluxed and stirred for 24 h under a N_2 atmosphere. The obtained solid was rinsed with toluene three times, filtered, and vacuum dried. The product was abbreviated as ZrP-SH, which was subsequently oxidized by 30 wt % H_2O_2 and 37 wt % HCl to form sulfonic acid groups,[16,38] i.e., ZrP-SO_3H, during

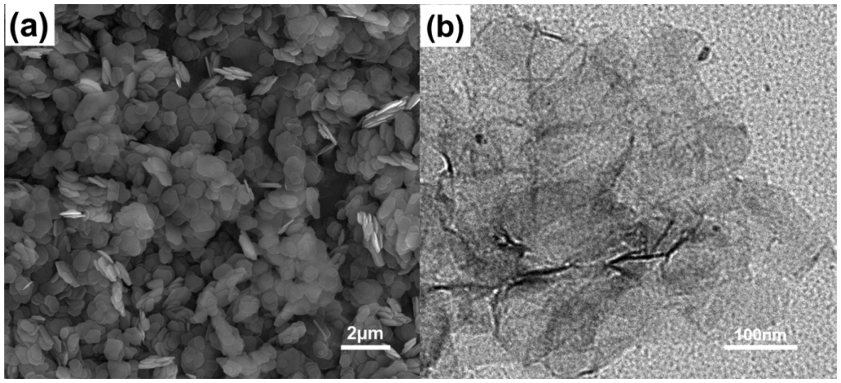

Figure 1. (a) SEM image of the ZrP microcrystals; (b) TEM image of the exfoliated ZrP nanosheets.

which 5.5 mL of H_2O_2 was dropwisely added to the dispersion of 0.30 g of ZrP-SH in 12.0 mL of methanol. The reaction was carried out at room temperature for 24 h. The obtained solid was further treated with 5.0 mL of 37 wt % HCl at ambient temperature for complete protonation. The sample was separated by centrifugation and then rinsed by water and ethanol. After being vacuum dried and ground, ZrP-SO_3H was obtained. The entire process to form acid functionalized ZrP single layer nanosheets is illustrated in Scheme 1.

2.4. Characterization. Fourier transform infrared spectroscopy (FTIR) spectra of samples were recorded on an Analect RFX-65A type FTIR spectrophotometer using KBr pellet samples. The KBr pallets were prepared by grinding spectroscopic grade KBr with 0.1 wt % of sample.

The thermal properties of the samples were characterized by a thermogravimetric analyzer (TGA, TA Instruments model Q50) under an air atmosphere (40 mL/min) at a heating rate of 10 °C/min.

The acidity of the samples was calculated from the pH value of 0.050 g solid particles dispersed in 5.0 mL of deionized water. The pH values were obtained from an Accument AB15 pH meter.

The X-ray photoelectron spectra (XPS) were collected on an ESCALAB250 (Thermo-VG Scientific) spectrometer. A monochromatized Al Kα (1486.6 eV, 15 kV, and 150 W) source was used. The spectra were recorded with a pass energy of 100 eV, and the C 1s line (284.6 eV) was used as a reference to adjust the electrostatic charging.

The X-ray diffraction (XRD) patterns were obtained on a Bruker D8 diffractometer with Bragg-Brentano θ-2θ geometry (40 kV and 30 mA), using graphite monochromatized Cu Kα radiation.

Surface morphology of the samples was recorded on an FEI Helios NanoLab 400 DualBeam scanning electron microscope (SEM) operated at 15 kV.

The porous properties of the samples were determined by a NOVE 1000 Surface Area Analyzer. The specific surface area (S_{BET}, m^2/g) was estimated based on the N_2 adsorption at the liquid nitrogen temperature. The samples were degassed at 150 °C for 2 h prior to each measurement.

2.5. Catalysis Evaluation. The Baeyer–Villiger oxidation of cyclohexanone to ε-caprolactone by H_2O_2 was carried out in a round-bottomed flask fitted with a condenser. Cyclohexanone (4.0 mmol), 30 wt % H_2O_2 aqueous solution (10.0 mmol), 4.0 mL acetonitrile, and an appropriate amount of ZrP-SO_3H were charged into the reactor. The reaction was carried out at 80 °C for a pre-terminated duration. The products were analyzed by a gas chromatography/mass spectrometers (GC/MS) (Hewlett Packard 5890 & 6890 Series).

3. RESULTS AND DISCUSSION

The prepared ZrP microcrystals and exfoliated ZrP single layer nanosheets were studied by SEM and TEM and are shown in Figure 1. According to the SEM image, the ZrP microcrystals exhibit a roughly hexagonal shape, indicating its high crystallinity. After exfoliation by TBA, the layered ZrP microcrystals were separated into individual nanosheets,[20] as shown in Figure 1b.

Figure 2 presents the FTIR spectra of the ZrP micro-crystals and the grafted ZrP nanosheets. For the FTIR spectrum of ZrP

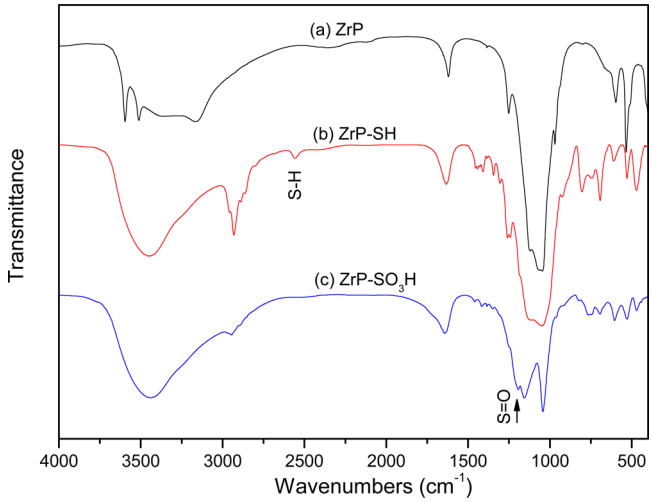

Figure 2. FTIR spectra of ZrP microcrystals and functionalized ZrP nanosheets.

micro-crystals shown in Figure 2a, the bands at 3512 and 3595 cm^{-1} are due to the water molecules in the interlayer space of ZrP,[39] while the bands at 3165 and 1620 cm^{-1} are from the symmetric and bending vibrations of −OH groups in ZrP, respectively. The peaks at 970 and 1251 cm^{-1} are attributed to the out-of-plane and in-plane vibration of the P−OH groups, respectively, whereas the other two IR bands located at 1047 and 1121 cm^{-1} are associated with the symmetric and asymmetric stretch of P−O in the PO_2 groups, respectively.[40] The two peaks at 534 and 593 cm^{-1} are ascribed to the vibration of Zr−O.[41] According to the FTIR spectrum of ZrP-SH presented in Figure 2b, the bands located at 2932, 2558, 1120, and 472 cm^{-1} belong to the C−H stretching, S−H stretching, Si−O bending and symmetric stretching vibrations, respectively, suggesting the existence of MTPMS moieties in the grafted ZrP nanosheets. Furthermore, the out-of-plane vibration mode of P−OH groups at 970 cm^{-1} in pristine ZrP shifted to 923 cm^{-1} in ZrP-SH, suggesting a successful condensation reaction between Si−OCH_3 groups of MTPMS and P−OH groups of ZrP nanosheets. The above results have clearly shown that MTPMS has been covalently grafted onto ZrP nanosheets surface. In the FTIR spectrum of ZrP-SO_3H in

dx.doi.org/10.1021/am5008408 | ACS Appl. Mater. Interfaces 2014, 6, 7417−7425

Figure 2c, the peak related to S−H in ZrP-SH at 2558 cm^{-1} disappeared and a new peak associated with S═O at 1195 cm^{-1} appeared. These changes indicate that the thiol groups have been oxidized to sulfonic acid groups.[42] In addition, the peak located at 1044 cm^{-1} in the spectrum of ZrP-SO_3H could be assigned to the overlap of the stretching vibrations of S═O and P−O bonds.

The thermal decomposition of the pristine ZrP microcrystals and functionalized ZrP nanosheets were studied by thermogravimetric analysis (TGA), and the results are displayed in Figure 3. Each sample was treated at 100 °C for 30 min in an

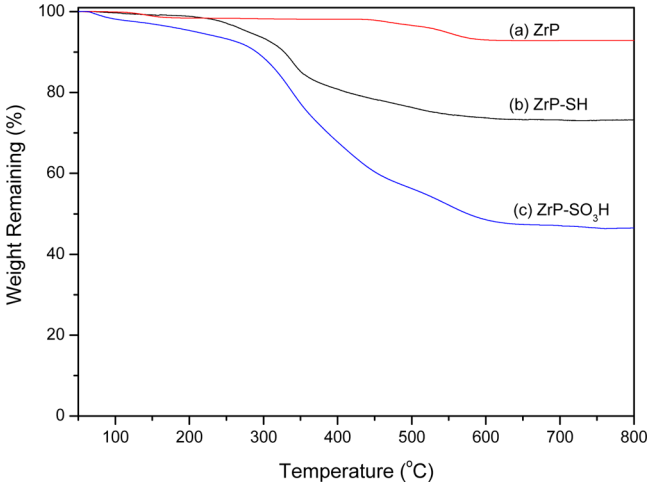

Figure 3. TGA thermograms of ZrP microcrystals and functionalized ZrP nanosheets.

argon flow to remove the absorbed moisture, and then it was cooled down to 50 °C to start the thermal analysis. Two major weight losses in 100−170 and 420−600 °C range were observed in the pristine ZrP micro-crystals (Figure 3a). They correspond to the loss of hydration water and condensation water in ZrP, respectively.[26] As it is shown in Figure 3b, a total weight loss of ca. 26.8 wt % was recorded by two steps in regions of 180−420 and 420−700 °C, which were due to the step by step thermal decomposition of the thiol groups and the remaining grafted organic moiety in ZrP-SH, respectively, as determined by their corresponding molecular weight. For ZrP-SO_3H (Figure 3c), a small amount of weight loss below 100 °C was observed. This is believed owing to the loss of water, because −SO_3H groups have a high hydrophobicity and thus it is hard to completely dry the sample. The two steps of major weight loss at 140−450 and 450−700 °C can be assigned to the thermal dissociation of surface sulfonic acid groups and the remaining organic chains, and the entire weight loss was 53.6 wt %.

The XPS survey scan profiles of ZrP microcrystals, ZrP-SH, and ZrP-SO_3H are presented in Figure 4. The existence of S and Si elements on the surface of ZrP-SH confirmed the successful grafting of thiol terminated chains on the ZrP nanosheets. The peak intensity ratio of Zr and C elements in ZrP-SH and ZrP-SO_3H became weaker compared to that of ZrP. Meanwhile, the S and Si peaks exhibited relatively high intensity. Considering XPS is a very surface sensitive technique, these observations suggest that ZrP nanosheets were covered after surface grafting. The high resolution XPS spectra of P 2p were recorded and are shown in Figures 5. The binding energy of the P 2p peak of ZrP-SH shifted to a lower value after the

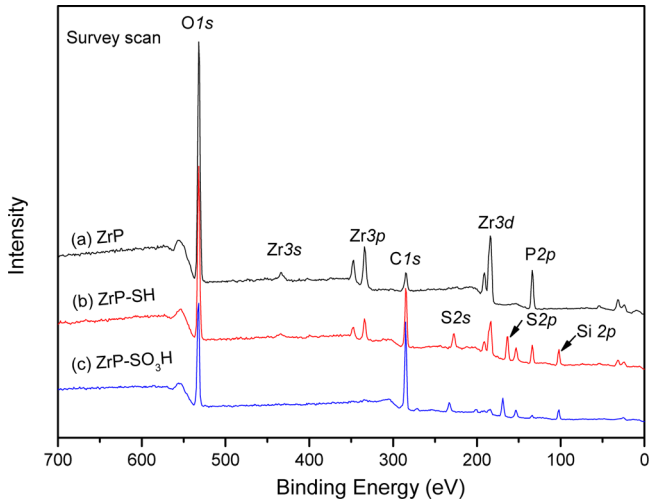

Figure 4. XPS survey scan of ZrP microcrystals and functionalized ZrP nanosheets.

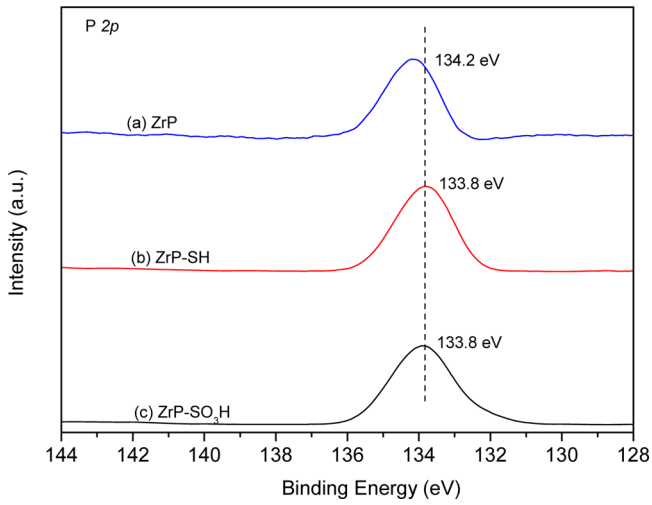

Figure 5. High-resolution XPS P 2p peaks of (a) ZrP, (b) ZrP-SH, and (c) ZrP-SO_3H.

grafting reaction. This result is consistent with the formation of P−O−Si bonds from the condensation reaction between the hydroxyl groups on the surface of ZrP nanosheets and the silane groups of MTPMS, which was also verified by the FTIR characterization (Figure 2). The binding energy of P 2p did not change after ZrP-SH was oxidized into ZrP-SO_3H. This result indicates that the oxidation treatment of ZrP-SH did not affect the chemical bonds between the ZrP nanosheets and the grafted chains, ensuring that the chains remained grafted on the ZrP nanosheets surface after oxidation treatment.

To further verify that the thiol groups were indeed oxidized into sulfonic acid groups under the treatment of H_2O_2 and HCl, high-resolution XPS spectra of S were recorded, and the results are shown in Figure 6. The binding energy of S 2p3/2 in ZrP-SH shifted to a higher binding energy after the oxidation treatment, which supports that the thiol groups were oxidized into sulfonic acid groups, which is also highly consistent with the FTIR (Figure 2) and TGA (Figure 3) characterization results.

On the basis of the TGA and XPS results, one can estimate the degree of functionalization on the surface of ZrP nanosheets. The distance of the neighboring hydroxyl groups

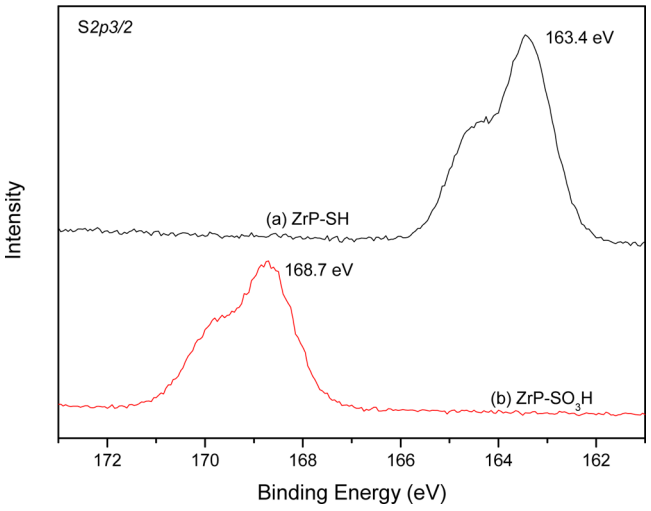

Figure 6. High-resolution XPS S 2p3/2 peaks of (a) ZrP-SH and (b) ZrP-SO_3H.

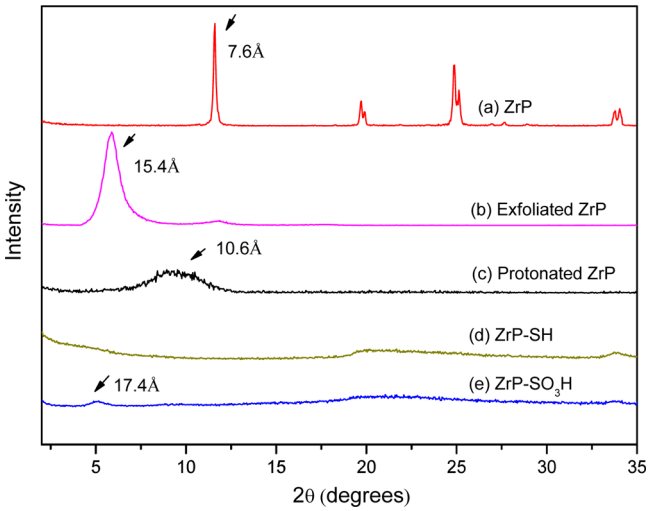

Figure 7. XRD patterns of ZrP and functionalized ZrP nanosheets.

on ZrP nanosheets surface is at least 4.53 Å apart,[21] larger than twice of the bond length of Si−O in silane.[43,44] Thus, one MPTMS cannot bridge on multiple hydroxyl groups. As such, based on the weight loss difference between the ZrP and ZrP-SH (Figure 3), the degree of surface functionalization is estimated to be ca. 58%. This value is also consistent with the estimation based on the weight loss difference between the Zr-SH and ZrP-SO_3H assuming that all −SH groups were oxidized to be $-SO_3H$ groups, which is supported by the XPS characterization results as shown in Figure 6.

The pH values and calculated acidities of ZrP microcrystals and functionalized ZrP nanosheets are presented in Table 1.

Table 1. Acidity of ZrP Microcrystals and Functionalized ZrP Nanosheets

	ZrP	ZrP-SH	ZrP-SO_3H
pH value	5.0	6.6	1.7
acidity (μmol/g)	0.5	0.0126	100

The acidity of ZrP microcrystals is mainly contributed by the hydroxyl groups within ZrP layers.[45] When thiol group terminated chains were grafted onto ZrP single-layer nanosheets, the acidity of ZrP-SH decreased, indicating the successful condensation reaction between the hydroxyl groups of individual ZrP nanosheets and the methoxysilane groups of MPTMS. After the ZrP-SH nanosheets were oxidized to ZrP-SO_3H, the acidity was tremendously enhanced to 100 μmol/g, which in turn supports the formation of sulfonic acid groups.

Figure 7 presents the XRD patterns of ZrP microcrystals, exfoliated ZrP nanosheets, protonated ZrP nanosheets, ZrP-SH and ZrP-SO_3H. ZrP microcrystals were tested in a powder form while the remaining samples were cast and dried on a silicon wafer for XRD characterization. The formation of crystalline ZrP with an interlayer distance of 7.6 Å[20,22−25] can be confirmed from the XRD pattern presented in Figure 7a. The XRD patterns shown in panels b and c in Figure 7 are exfoliated ZrP nanosheets and the subsequently protonated ZrP gel after drying and re-stacking on a silicon wafer, respectively. For the exfoliated ZrP nanosheets, a new diffraction peak at ca. 5.8° (d = 15.4 Å) appeared, indicating that the exfoliated ZrP nanosheets can restack to form an ordered layered structure with an interlayer distance of ca. 15.4 Å.[22,30] The increased interlayer distance is owing to the sandwiching of TBA cations between individual nanosheets.[30] The acid treatment can recover the surface hydroxyl groups on the ZrP nanosheets and release TBA cations. The protonated ZrP nanosheets tended to form a gel because of the strong hydrogen bonding between layers together with water molecules. When the ZrP nanosheets gel was dried, a loosely ordered layered structure formed, as indicated by the broad diffraction peak located at ca. 9.3° (d = 10.6 Å, Figure 7c).[38] After the side chains were grafted onto ZrP nanosheets surface, the side chains led to irregular surface of the nanosheets, which are not favorable for the restacking of the nanosheets. As such, no diffraction peaks corresponding to the ordered layered structure were observed in the XRD patterns of ZrP-SH (Figure 7d), which indicates that the grafting of thiol group terminated side chains on ZrP nanosheets resulted in random arrangement of the individual nanosheets. After the thiol terminating groups were oxidized to sulfonic acid groups, a weak peak at ca. 5.1° (d = 17.4 Å, Figure 7e) appeared in the dried ZrP-SO_3H nanosheets, suggesting that the nanosheets restacked into a loosely ordered layered structure. This is probably owing to the weak interaction between the sulfonic acid groups at neighboring ZrP nanosheets. The increased interlayer distance is due to the grafted side chains.

The random stacking of nanosheets is expected to form a porous structure. Thus, the potential porous properties of the restacked functionalized ZrP nanosheets were investigated and the results are summarized in Table 2. As expected, the degree of randomness of individual nanosheets arrangement exhibited a good correlation with the surface area. The most randomly stacked ZrP-SH nanosheets possess the highest surface area of 129.2 m^2/g, higher than that of the loosely stacked ZrP-SO_3H nanosheets. Although the well-stacked ZrP microcrystals

Table 2. Surface Area of ZrP and Functionalized ZrP Nanosheets

sample	S_{BET} (m^2/g)
ZrP microcrystals	27.5
ZrP-SH	129.2
ZrP-SO_3H	40.8

dx.doi.org/10.1021/am5008408 | ACS Appl. Mater. Interfaces 2014, 6, 7417−7425

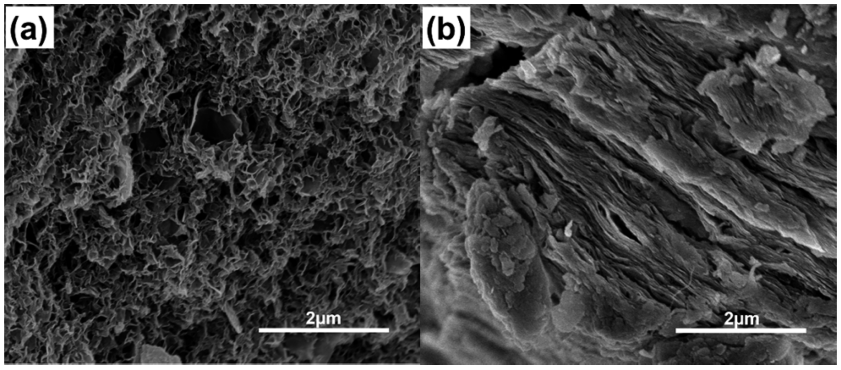

Figure 8. SEM images of the restacked and dried (a) ZrP-SH and (b) ZrP-SO_3H nanosheets.

possess the lowest surface area. To be noted, the surface area of ZrP-SO_3H listed in Table 2 is the surface area of the dried and restacked nanosheets (as shown in Figure 8b). It does not represent the surface area of ZrP-SO_3H nanosheets in the dispersed state, which should be much higher (although it is hard to test it in the dispersed state).

The microstructure of the restacked ZrP-SH and ZrP-SO_3H nanosheets was recorded under SEM and are presented in Figure 8. Apparently, ZrP-SH sample exhibited a porous structure, in high contrast to the crystalline hexagonal pristine ZrP micro-crystals as shown in Figure 1A, whereas the ZrP-SO_3H sample presented a roughly layered morphology. These results are highly consistent with the XRD analysis (Figure 7) and porous properties (Table 2) discussed above. The roughly layered structure of the restacked ZrP-SO_3H nanosheets is probably owing to the hydrogen bonding between the sulfonic acid groups at neighboring ZrP nanosheets and water molecules within layers. Such weak interactions help guide the stacking of nanosheets. In contrast, lack of such a weak interaction between ZrP-SH nanosheets led to the random stacking of ZrP-SH nanosheets, resulting in a porous structure.

It should be noted that ZrP-SO_3H nanosheets can be well-dispersed in polar solvents or reactants, enabling the sulfonic acid groups to be highly accessible, which is very critical for many applications, such as catalysis.

Bayer−Villiger oxidation is a fundamental organic reaction in converting ketones into esters or lactones by oxidative transformation using a mixture of persulfate and concentrated sulfuric acid.[46] This reaction has been widely studied as a powerful tool to prepare natural products (e.g., antibiotics, steroids, pheromones) or monomers.[47] Huge efforts have been devoted to seek environmentally friendly oxidants along with recyclable catalysts for Bayer-Villiger oxidation.[48] The most frequently used oxidants are organic peracids and peroxides, but they suffer from producing waste by-products and potentially generating explosive dangers. Besides, they are not economically viable for industrial applications.[49] The direct use of H_2O_2 as the oxidant has been the most promising alternative to these organic peracids and peroxides because H_2O_2 contains a high concentration of active oxygen (47 wt %) and is inexpensive, commercially available, and environmentally friendly.[50] Up to now, many heterogeneous catalysts such as titanium- and tin-containing zeolites,[51−53] polymer-anchored metal complexes,[48,54,55] cationic or anionic clay-based catalysts,[50,56−60] and polymers with sulfonic acid groups[61] have been explored for the Baeyer−Villiger oxidation with H_2O_2 as an oxidant. However, these catalysts usually have serious weaknesses including their low selectivity, leaching of active components to the reaction system, and short lifetime.[47,52,62,63] Furthermore, these catalytic systems involve the usage of various toxic organic solvents including dichloromethane, carbon tetrachloride, benzene, and acetonitrile. These issues prohibit their practical applications in large-scale industrial process. Hence, it is highly desirable to develop new reaction systems including oxidants, catalysts, and solvents with low cost and environmentally friendly nature for the Bayer−Villiger oxidation.

The acid functionality is very important for the Bayer−Villiger oxidation according to its mechanism.[47] The sulfonic acid grafted ZrP nanosheets are of high acidity (as shown in Table 1) and heterogeneous, rendering it promising for the Bayer−Villiger oxidation. Therefore, it is evaluated as a catalyst for the Baeyer-Villiger oxidation of cyclohexanone to ε-caprolactone by H_2O_2 under various conditions. The influence of catalyst amount on the catalytic activity is presented in Figure 9. With an increasing amount of catalyst, the ε-caprolactone yield first increased gradually up to ca. 83.3%, and then decreased with a further increase in the catalyst loading. The optimum amount of ZrP-SO_3H solid catalyst is 0.20 g under the reaction condition of 4.0 mmol cyclohexanone, 10.0 mmol H_2O_2, and 4.0 mL CH_3CN as solvent for 24 h.

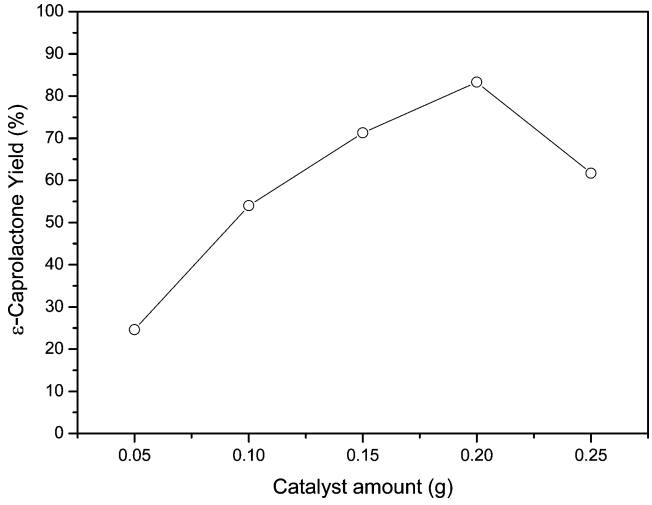

Figure 9. Effect of catalyst loading on the catalytic performance.

Based on the optimized catalyst loading, Figure 10 presents the catalytic reaction evaluation results as a function of reaction time and solvent. It was found that the ε-caprolactone yield initially increased steadily with an extended reaction time and then leveled off at around 80% after 12 h of reaction for the

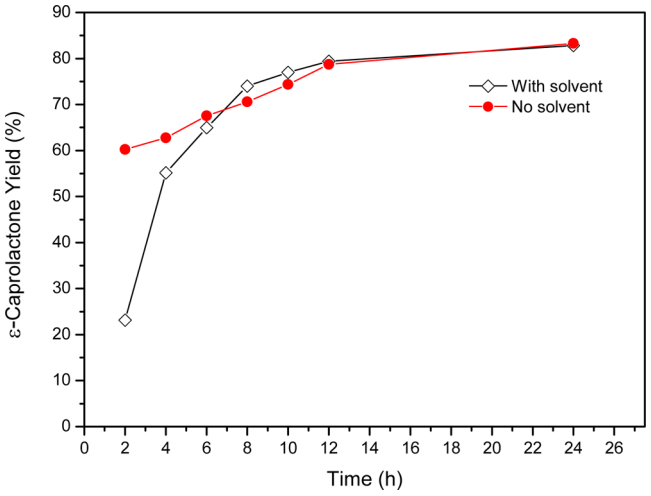

Figure 10. Influences of reaction time and solvent on the catalytic activity of ZrP-SO_3H (0.20 g of catalysts).

reaction systems both with and without CH_3CN as a solvent. It is expected that after an extended period of reaction, similar yield would be achieved regardless whether a solvent was used or not, considering eventually the reaction will reach equilibrium. On the other hand, during the first 6 h, it was clearly observed that the ε-caprolactone yield in the reaction system with solvent CH_3CN was lower than that without CH_3CN. This is because ZrP-SO_3H nanosheets are hydrophilic, which could be well-dispersed in the water-rich environment with limited or no organic solvent. This in turn results in a high degree of exposure of sulfonic acid groups. Considering the cost, toxicity, and the added complexity of any organic solvent involved reaction, eliminating solvent while still maintaining high reaction yield is highly desirable for most industrial processes. Therefore, the ZrP-SO_3H solid acid may bring extra benefits when used as a heterogeneous catalyst in industry.

Because ZrP-SO_3H is a solid acid, it can be easily separated from the reaction system by centrifugation (4 min at 9600 G force) and reused for the next catalytic run. The dispersion and separation of ZrP-SO_3H nanosheets in the reaction system is presented in Figure 11. ZrP-SO_3H nanosheets are initially in a form of fine powders (Figure 11a). It could be uniformly dispersed in the reaction system (Figure 11b). After the reaction, ZrP-SO_3H can be collected by centrifugation as a form of gel (Figure 11c), which can be easily re-dispersed in the reaction system for the next run (Figure 11d).

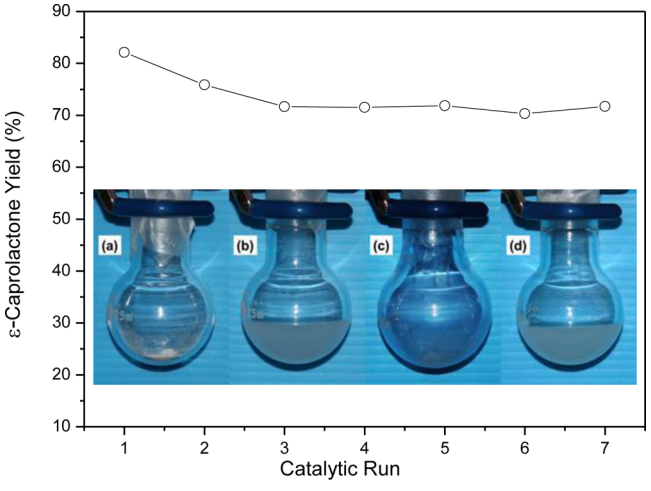

Figure 11. Demonstration of recycling of ZrP-SO_3H nanosheets in the reaction system (the inset) and recyclability of ZrP-SO_3H (0.20 g of catalyst).

The recyclability of ZrP-SO_3H was investigated, and the results are presented in Figure 11. The ε-caprolactone yield decreased slightly during the first 3 cycles of reaction, and then it leveled off to ca. 71% until the 7th cycle. The slight drop of catalytic performance during the first few runs is probably owing to the loss of a small amount of non-covalently bonded chains that are attached to the sheet surface. The stable catalytic activity indicates that most sulfonic acid groups are tightly bonded with ZrP nanosheets, thanks to the covalent bonding strategy.

Many other heterogeneous catalyst systems have been explored for Baeyer–Villiger oxidation by H_2O_2, but most of these catalysts exhibited low activity and required a solvent. For example, Sn-doped hydrotalcite[49] led to a highest yield of 58% with CH_3CN as solvent, polystyrene resin supported tin complexes[64] achieved a yield less than 56% with 1,4-dioxane as solvent, and titanium silicate[51] supported Pt-complexes also showed low activity. The ZrP-SO_3H nanosheets in our research helped achieve a high ε-caprolactone yield up to ca. 83.3%. In addition, the ZrP-SO_3H nanosheets could perform well even without CH_3CN as solvent. The above evaluation results demonstrate that ZrP-SO_3H nanosheets are an excellent candidate for commercial exploration in Baeyer–Villiger oxidation.

Although only the Baeyer–Villiger oxidation of cyclohexanone to ε-caprolactone was selected for the evaluation here, it is believed that such a strong solid acid can find wide applications anywhere acid can serve as a catalyst, particularly in a hydrophilic reaction system, including transesterification reactions,[65] Peckmann reactions.[66] In addition, such a strong solid acid may find other applications that requires both high acidity and a heterogeneous system, such as fuel cell membranes,[67] separation technologies,[68] etc.

4. CONCLUSION

A strong solid acid was successfully prepared by covalently anchoring sulfonic acid group terminated chains on individual ZrP single layer nanosheets. The solid acid based on ZrP nanosheets with a high loading density of sulfonic acid groups can be well dispersed in a polar reaction media, enabling the acid functional groups to be highly accessible. When they were applied as a catalyst for the Baeyer–Villiger oxidation of cyclohexanone to ε-caprolactone at 80 °C for 24 h, an ε-caprolactone yield of 83.3% was achieved. Furthermore, the ZrP-SO_3H nanosheets could be easily separated from the products and recycled up to at least 7 times without significant loss of catalytic activity. Therefore, ZrP-SO_3H nanosheets hold a great potential as a high-performance heterogeneous catalyst for acid catalyzed reactions.

AUTHOR INFORMATION

Corresponding Authors

* E-mail: luyi.sun@uconn.edu. Tel: (860) 486-6895. Fax: (860) 486-4745.
*E-mail: mengyzh@mail.sysu.edu.cn. Tel: (0086) 20-8411-4113. Fax: (0086) 20-8411-4113.

Notes

The authors declare no competing financial interest.

■ ACKNOWLEDGMENTS

This research is sponsored by the National Science Foundation (Partnerships for Research and Education in Materials, DMR-1205670), the Air Force Office of Scientific Research (FA9550-12-1-0159), Cottrell College Science Award from the Research Corporation for Science Advancement (Award 19770), the Faculty Large Grant from the University of Connecticut, and a grant from The Key Laboratory of Low-carbon Chemistry & Energy Conservation of Guangdong Province. Y.Z. acknowledges the China Scholarship Council for offering her a scholarship to conduct research at University of Connecticut.

■ REFERENCES

(1) Kitano, M.; Nakajima, K.; Kondo, J. N.; Hayashi, S.; Hara, M. Protonated Titanate Nanotubes as Solid Acid Catalyst. *J. Am. Chem. Soc.* **2010**, *132* (19), 6622−6623.

(2) Xu, T.; Kob, N.; Drago, R. S.; Nicholas, J. B.; Haw, J. F. A Solid Acid Catalyst at the Threshold of Superacid Strength: NMR, Calorimetry, and Density Functional Theory Studies of Silica-supported Aluminum Chloride. *J. Am. Chem. Soc.* **1997**, *119* (50), 12231−12239.

(3) Corma, A. Solid Acid Catalysts. *Curr. Opin Solid State Mater. Sci.* **1997**, *2* (1), 63−75.

(4) Molnar, A. Nafion-silica Nanocomposites: A New Generation of Water-Tolerant Solid Acids of High Efficiency. *Curr. Org. Chem.* **2008**, *12* (2), 159−181.

(5) Gelbard, G. Organic Synthesis by Catalysis with Ion-Exchange Resins. *Ind. Eng. Chem. Res.* **2005**, *44* (23), 8468−8498.

(6) Corma, A. Inorganic Solid Acids and Their Use in Acid-Catalyzed Hydrocarbon Reactions. *Chem. Rev.* **1995**, *95* (3), 559−614.

(7) Anastas, P. T.; Kirchhoff, M. M. Origins, Current Status, and Future Challenges of Green Chemistry. *Acc. Chem. Res.* **2002**, *35* (9), 686−694.

(8) Macht, J.; Carr, R. T.; Iglesia, E. Functional Assessment of the Strength of Solid Acid Catalysts. *J. Catal.* **2009**, *264* (1), 54−66.

(9) Carr, R. T.; Neurock, M.; Iglesia, E. Catalytic Consequences of Acid Strength in the Conversion of Methanol to Dimethyl Ether. *J. Catal.* **2011**, *278* (1), 78−93.

(10) Simonetti, D. A.; Carr, R. T.; Iglesia, E. Acid Strength and Solvation Effects on Methylation, Hydride Transfer, and Isomerization Rates During Catalytic Homologation of C-1 Species. *J. Catal.* **2012**, *285* (1), 19−30.

(11) Barbaro, P.; Liguori, F. Ion Exchange Resins: Catalyst Recovery and Recycle. *Chem. Rev.* **2009**, *109* (2), 515−529.

(12) Harmer, M. A.; Sun, Q. Solid Acid Catalysis Using Ion-exchange Resins. *Appl. Catal. A* **2001**, *221* (1-2), 45−62.

(13) Lam, E.; Majid, E.; Leung, A. C. W.; Chong, J. H.; Mahmoud, K. A.; Luong, J. H. T. Synthesis of Furfural From Xylose by Heterogeneous and Reusable Nafion Catalysts. *ChemSusChem* **2011**, *4* (4), 535−541.

(14) Harmer, M. A.; Farneth, W. E.; Sun, Q. High Surface Area Nafion Resin/silica Nanocomposites: A New Class of Solid Acid Catalyst. *J. Am. Chem. Soc.* **1996**, *118* (33), 7708−7715.

(15) Park, J. W.; Park, Y. J.; Jun, C. H. Post-grafting of Silica Surfaces with Pre-functionalized Organosilanes: New Synthetic Equivalents of Conventional Trialkoxysilanes. *Chem. Commun.* **2011**, *47* (17), 4860−4871.

(16) Cano-Serrano, E.; Campos-Martin, J. M.; Fierro, J. L. G. Sulfonic Acid-functionalized Silica Through Quantitative Oxidation of Thiol Groups. *Chem. Commun.* **2003**, *2*, 246−247.

(17) Rhee, C. H.; Kim, H. K.; Chang, H.; Lee, J. S. Nafion/sulfonated Montmorillonite Composite: A New Concept Electrolyte Membrane for Direct Methanol Fuel Cells. *Chem. Mater.* **2005**, *17* (7), 1691−1697.

(18) Smuleac, V.; Butterfield, D. A.; Sikdar, S. K.; Varma, R. S.; Bhattacharyya, D. Polythiol-functionalized Alumina Membranes for Mercury Capture. *J. Membr. Sci.* **2005**, *251* (1-2), 169−178.

(19) Felice, V.; Ntais, S.; Tavares, A. C. Propyl Sulfonic Acid Functionalization of Faujasite-type Zeolites: Effect on Water and Methanol Sorption and on Proton Conductivity. *Microporous Mesoporous Mater.* **2013**, *169*, 128−136.

(20) Sun, L. Y.; Boo, W. J.; Browning, R. L.; Sue, H. J.; Clearfield, A. Effect of Crystallinity on the Intercalation of Monoamine in Alpha-zirconium Phosphate Layer Structure. *Chem. Mater.* **2005**, *17* (23), 5606−5609.

(21) Troup, J. M.; Clearfield, A. On the Mechanism of Ion Exchange in Zirconium Phosphates. 20. Refinement of the Crystal Structure of a-zirconium Phosphate. *Inorg. Chem.* **1977**, *16* (12), 3311−3314.

(22) Sun, L.; Boo, W. J.; Sue, H.-J.; Clearfield, A. Preparation of Alpha-zirconium Phosphate Nanoplatelets with Wide Variations in Aspect Ratios. *New J. Chem.* **2007**, *31* (1), 39−43.

(23) Alberti, G. Syntheses, Crystalline-structure, and Ion-exchange Properties of Insoluble Acid Salts of Tetravalent Metals and Their Salt Forms. *Accounts Chem. Res.* **1978**, *11* (4), 163−170.

(24) Clearfield, A. Inorganic-ion Exchangers with Layered Structures. *Annu. Rev. Mater. Sci.* **1984**, *14*, 205−229.

(25) Clearfield, A. Group-IV Phosphates as Catalysts and Catalyst Supports. *J. Mol. Catal* **1984**, *27* (1-2), 251−262.

(26) Hu, H.; Martin, J. C.; Xiao, M.; Southworth, C. S.; Meng, Y. Z.; Sun, L. Y. Immobilization of Ionic Liquids in Layered Compounds via Mechanochemical Intercalation. *J. Phys. Chem. C* **2011**, *115* (13), 5509−5514.

(27) Boo, W. J.; Sun, L.; Liu, J.; Clearfield, A.; Sue, H.-J. Effective Intercalation and Exfoliation of Nanoplatelets in Epoxy via Creation of Porous Pathways. *J. Phys. Chem. C* **2007**, *111* (28), 10377−10381.

(28) Alberti, G.; Casciola, M.; Capitani, D.; Donnadio, A.; Narducci, R.; Pica, M.; Sganappa, M. Novel Nafion-zirconium Phosphate Nanocomposite Membranes with Enhanced Stability of Proton Conductivity at Medium Temperature and High Relative Humidity. *Electrochim. Acta* **2007**, *52* (28), 8125−8132.

(29) Hu, H.; Martin, J. C.; Zhang, M.; Southworth, C. S.; Xiao, M.; Meng, Y. Z.; Sun, L. Y. Immobilization of Ionic Liquids in Theta-zirconium Phosphate for Catalyzing the Coupling of CO_2 and Epoxides. *RSC Adv.* **2012**, *2* (9), 3810−3815.

(30) Sun, L. Y.; Boo, W. J.; Sun, D. H.; Clearfield, A.; Sue, H. J. Preparation of Exfoliated Epoxy/alpha-zirconium Phosphate Nanocomposites Containing High Aspect Ratio Nanoplatelets. *Chem. Mater.* **2007**, *19* (7), 1749−1754.

(31) Sue, H.-J.; Gam, K. T.; Bestaoui, N.; Spurr, N.; Clearfield, A. Epoxy Nanocomposites Based on the Synthetic α-zirconium Phosphate Layer Structure. *Chem. Mater.* **2004**, *16* (2), 242−249.

(32) Sue, H.-J.; Gam, K. T.; Bestaoui, N.; Clearfield, A.; Miyamoto, M.; Miyatake, N. Fracture Behavior of α-zirconium Phosphate-based Epoxy Nanocomposites. *Acta Mater.* **2004**, *52* (8), 2239−2250.

(33) Wei, S. Y.; Lizu, M.; Zhang, X.; Sampathi, J.; Sun, L. Y.; Milner, M. F. Electrospun Poly(vinyl alcohol)/alpha-zirconium Phosphate Nanocomposite Fibers. *High Perform. Polym.* **2013**, *25* (1), 25−32.

(34) Gao, Y.; Zhang, Z.; Wu, J.; Duan, L.; Umar, A.; Sun, L.; Guo, Z.; Wang, Q. A Critical Review on the Heterogeneous Catalytic Oxidation of Elemental Mercury in Flue Gases. *Environ. Sci. Technol.* **2013**, *47* (19), 10813−10823.

(35) Sun, L. Y.; Boo, W. J.; Clearfield, A.; Sue, H. J.; Pham, H. Q. Barrier Properties of Model Epoxy Nanocomposites. *J. Membrane Sci.* **2008**, *318* (1-2), 129−136.

(36) Boo, W. J.; Sun, L. Y.; Liu, J.; Moghbelli, E.; Clearfield, A.; Sue, H. J.; Pham, H.; Verghese, N. Effect of Nanoplatelet Dispersion on Mechanical Behavior of Polymer Nanocomposites. *J. Polym. Sci. Polym. Phys.* **2007**, *45* (12), 1459−1469.

(37) Alberti, G.; Casciola, M.; Pica, M.; Di Cesare, G. Preparation of Nano-structured Polymeric Proton Conducting Membranes for Use in Fuel Cells. *Ann. NY Acad. Sci.* **2003**, *984*, 208−225.

(38) Alberti, G.; Casciola, M.; Costantino, U. Inorganic Ion-exchange Pellicles Obtained by Delamination of Alpha-zirconium Phosphate Crystals. *J. Colloid Interface Sci.* **1985**, *107* (1), 256−263.
(39) Huisken, F.; Kaloudis, M.; Kulcke, A. Infrared Spectroscopy of Small Size-selected Water Clusters. *J. Chem. Phys.* **1996**, *104*, 17−25.
(40) Koleva, V.; Stefov, V.; Cahil, A.; Najdoski, M.; Šoptrajanov, B.; Engelen, B.; Lutz, H. D. Infrared and Raman Studies of Manganese Dihydrogen Phosphate Dihydrate, $Mn(H_2PO_4)_2$ $2H_2O$. I: Region of the Vibrations of the Phosphate Ions and External Modes of the Water Molecules. *J. Mol. Struct* **2009**, *917* (2-3), 117−124.
(41) Barraclough, C. G.; Bradley, D. C.; Lewis, J.; Thomas, I. M. The Infrared Spectra of Some Metal Alkoxides, Trialkylsilyloxides, and Related Silanols. *J. Chem. Soc.* **1961**, *0*, 2601−2605.
(42) Rostamizadeh, S.; Azad, M.; Shadjou, N.; Hasanzadeh, M. (α-Fe_2O_3)-MCM-41-SO_3H as a Novel Magnetic Nanocatalyst for the Synthesis of N-aryl-2-amino-1,6-naphthyridine Derivatives. *Catal. Commun.* **2012**, *25*, 83−91.
(43) Pereira, J.; Catlow, C.; Price, G. Ab Initio Studies of Silica-based Clusters. Part I. Energies and Conformations of Simple Clusters. *J. Phys. Chem. A* **1999**, *103* (17), 3252−3267.
(44) Pereira, J.; Catlow, C.; Price, G. Ab Initio Studies of Silica-based Clusters. Part II. Structures and Energies of Complex Clusters. *J. Phys. Chem. A* **1999**, *103* (17), 3268−3284.
(45) Alberti, G.; Casciola, M.; Palombari, R. Acid Zirconium-phosphates and Phosphonates as Proton Conductors and Their Use for Solid-State Gas Sensors. *Russ. J. Electrochem.* **1993**, *29* (12), 1257−1264.
(46) Renz, M.; Meunier, B. 100 years of Baeyer-Villiger Oxidations. *Eur. J. Org. Chem.* **1999**, *4*, 737−750.
(47) Jimenez-Sanchidrian, C.; Ruiz, J. R. The Baeyer-Villiger Reaction on Heterogeneous Catalysts. *Tetrahedron* **2008**, *64* (9), 2011−2026.
(48) Li, C. L.; Wang, J. Q.; Yang, Z. W.; Hu, Z. G.; Lei, Z. Q. Baeyer-Villiger Oxidation of Ketones with Hydrogen Peroxide Catalyzed by Cellulose-supported Dendritic Sn Complexes. *Catal. Commun.* **2007**, *8* (8), 1202−1208.
(49) Pillai, U. R.; Sahle-Demessie, E. Sn-exchanged Hydrotalcites as Catalysts for Clean and Selective Baeyer-Villiger Oxidation of Ketones using Hydrogen Peroxide. *J. Mol. Catal. A: Chem.* **2003**, *191* (1), 93−100.
(50) Chen, C. X.; Peng, J. S.; Li, B.; Wang, L. L. The Catalytic Baeyer-Villiger Oxidation of Cyclohexanone to Epsilon-caprolactone Over Stibium-containing Hydrotalcite. *Catal. Lett.* **2009**, *131* (3-4), 618−623.
(51) Bhaumik, A.; Kumar, P.; Kumar, R. Baeyer-Villiger Rearrangement Catalysed by Titanium Silicate Molecular Sieve (TS-1)/H2O2 System. *Catal. Lett.* **1996**, *40* (1-2), 47−50.
(52) Corma, A.; Nemeth, L. T.; Renz, M.; Valencia, S. Sn-zeolite Beta as a Heterogeneous Chemoselective Catalyst for Baeyer-Villiger Oxidations. *Nature* **2001**, *412* (6845), 423−425.
(53) Corma, A.; Navarro, M. T.; Nemeth, L.; Renz, M. Sn-MCM-41 a Heterogeneous Selective Catalyst for the Baeyer-Villiger Oxidation with Hydrogen Peroxide. *Chem. Commun.* **2001**, *21*, 2190−2191.
(54) Palazzi, C.; Pinna, F.; Strukul, G. Polymer-anchored Platinum Complexes as Catalysts for the Baeyer-Villiger Oxidation of Ketones: Preparation and Catalytic Properties. *J. Mol. Catal. A: Chem.* **2000**, *151* (1-2), 245−252.
(55) Bernini, R.; Coratti, A.; Fabrizi, G.; Goggiamani, A. CH3ReO3/H2O2 in Room Temperature Ionic Liquids: an Homogeneous Recyclable Catalytic System for the Baeyer-Villiger Reaction. *Tetrahedron Lett.* **2003**, *44* (50), 8991−8994.
(56) Lei, Z. Q.; Zhang, Q. H.; Wang, R. M.; Ma, G. F.; Jia, C. G. Clean and Selective Baeyer-Villiger Oxidation of Ketones with Hydrogen Peroxide Catalyzed by Sn-palygorskite. *J. Organomet. Chem.* **2006**, *691* (26), 5767−5773.
(57) Varma, R. S. Clay and Clay-supported Reagents in Organic Synthesis. *Tetrahedron* **2002**, *58* (7), 1235−1255.
(58) Vaccari, A. Clays and Catalysis: A Promising Future. *Appl. Clay Sci.* **1999**, *14* (4), 161−198.
(59) Pillai, U. R.; Sahle-Demessie, E. Oxidation of Alcohols Over Fe3+/Montmorillonite-K10 using Hydrogen Peroxide. *Appl. Catal. A* **2003**, *245* (1), 103−109.
(60) Sels, B. F.; De Vos, D. E.; Jacobs, P. A. Hydrotalcite-like Anionic Clays in Catalytic Organic Reactions. *Catal. Rev.* **2001**, *43* (4), 443−488.
(61) Fischer, J.; Holderich, W. F. Baeyer-Villiger-oxidation of Cyclopentanone with Aqueous Hydrogen Peroxide by Acid Heterogeneous Catalysis. *Appl. Catal. A* **1999**, *180* (1-2), 435−443.
(62) Strukul, G. Transition Metal Catalysis in the Baeyer−Villiger Oxidation of Ketones. *Angew. Chem., Int. Ed.* **1998**, *37* (9), 1198−1209.
(63) Corma, A.; Navarro, M. a. T.; Renz, M. Lewis Acidic Sn(IV) Centers-grafted onto MCM-41-as Catalytic Sites for the Baeyer−Villiger Oxidation with Hydrogen Peroxide. *J. Catal.* **2003**, *219* (1), 242−246.
(64) Zhang, Q.; Wen, S.; Lei, Z. Heterogeneous Baeyer−Villiger Oxidation of Ketones Using Hydrogen Peroxide as Oxidant Catalyzed by Aminomethyl Polystyrene Resin-supported Tin Complex. *React. Funct. Polym.* **2006**, *66* (11), 1278−1283.
(65) Liu, T.; Li, Z.; Li, W.; Shi, C.; Wang, Y. Preparation and Characterization of Biomass Carbon-based Solid Acid Catalyst for the Esterification of Oleic Acid with Methanol. *Bioresour. Technol.* **2013**, *133*, 618−621.
(66) Opanasenko, M.; Shamzhy, M.; Čejka, J. Solid Acid Catalysts for Coumarin Synthesis by the Pechmann Reaction: MOFs Versus Zeolites. *ChemCatChem.* **2013**, *5* (4), 1024−1031.
(67) Boysen, D. A.; Uda, T.; Chisholm, C. R.; Haile, S. M. High-Performance Solid Acid Fuel Cells Through Humidity Stabilization. *Science* **2004**, *303* (5654), 68−70.
(68) Clark, J. H. Solid Acids for Green Chemistry. *Acc. Chem. Res.* **2002**, *35* (9), 791−797.